JAAS

Analytical comparisons of handheld LIBS and XRF devices for rapid quantification of gallium in a plutonium surrogate matrix

Journal:	*Journal of Analytical Atomic Spectrometry*
Manuscript ID	JA-ART-11-2021-000404.R1
Article Type:	Paper
Date Submitted by the Author:	24-Jan-2022
Complete List of Authors:	Rao, Ashwin; Air Force Institute of Technology, Jenkins, Phillip; Air Force Institute of Technology, Auxier, John; Los Alamos National Laboratory, Actinide Analytical Chemistry Shattan, Michael; National Nuclear Security Administration Patnaik, Anil; Air Force Institute of Technology

Journal Name

ARTICLE TYPE

Cite this: DOI: 00.0000/xxxxxxxxxx

Analytical comparisons of handheld LIBS and XRF devices for rapid quantification of gallium in a plutonium surrogate matrix

Ashwin P. Rao,*[a] Phillip R. Jenkins,[a] John D. Auxier II,[b] Michael B. Shattan,[c] and Anil K. Patnaik[a]

Received Date
Accepted Date

DOI: 00.0000/xxxxxxxxxx

This work compares a portable laser-induced breakdown spectroscopy (LIBS) analyzer to a portable x-ray fluorescence (XRF) device for quantification of gallium (Ga) in a plutonium surrogate matrix of cerium (Ce) for the first time. Calibration methods are developed with spectra of Ce-Ga samples from both devices. Metrics such as limit of detection (LoD) and mean average percent error (*MAPE*) are examined to evaluate calibration performance. While the portable LIBS device can yield a nearly instantaneous analytical measurement, its accuracy is hampered by self-absorption. By employing a self-absorption correction and increasing gating delay, LIBS calibrations with errors in the low single percents and LoDs of 0.1% Ga were constructed. The XRF device produces calibrations with superlative sensitivity, yielding LoDs for gallium in the low tens of parts-per-million (ppm), two orders of magnitude lower than the corrected LIBS models. However, a clear trade-off of measurement fidelity is established between the instantaneous analysis of the LIBS device and the minutes-long XRF measurement yielding superior detection limits.

1 Introduction

The analysis of minor constituent elements in plutonium alloys poses a challenging chemical problem. Many properties of the metal including its radioactivity, pyrophoricity, and complex electronic structure render it significantly more difficult to subject to various chemical processes than most other metals[1]. Traditionally, inductively-coupled-plasma mass spectrometry (ICP-MS) or inductively-coupled-plasma optical emission spectroscopy (ICP OES) are implemented as a reliable solution to accurately quantify minor elements in plutonium alloys[2–4]. These methods can reliably yield accurate determinations of minor elements in a bulk sample with low limits of detection (LoDs) in fractions of parts-per-million (ppm)[5,6]. However, these techniques have certain drawbacks with respect to sample processing time. Extensive sample preparation procedures are often required, to include dissolving Pu metal in acid for periods of up to a few days. Additionally, the machinery required for these procedures entails a sample be moved to a separate facility for analysis, posing issues of radiation safety expenditures of time and money. These issues have garnered interest in investigating other chemical analysis techniques that can be conducted *in-situ* during different stages in Pu manufacturing and provide instantaneous chemical composition results with no extensive sample preparation requirements.

Portable, handheld analyzers that are employed for elemental analysis of a sample show great promise for the aforementioned application. Two specific techniques of interest are x-ray fluorescence (XRF) and laser-induced breakdown spectroscopy (LIBS)[7–9]. XRF directs x-rays at a target to induce fluorescence of the target atoms; the incident x-ray removes an inner shell electron, leaving a vacancy that is filled by an outer shell electron leaving its higher energy state. This transition emits fluorescent x-ray radiation at a characteristic energy which can be recorded and matched to a particular element. Alternatively, LIBS uses a pulsed laser to ablate the surface of a target and generate a microplasma; the optical emissions from electronic transitions as the plasma cools are recorded with a spectrometer and charged-coupled device (CCD) camera. Specific wavelengths in the recorded spectra then indicate the presence of particular elements in the target.

Both XRF and LIBS have demonstrated their utility in chemical composition quantification of many different types of materials including geological[10–15] and environmental samples[16–19]. Moreover, both techniques have been validated for use in nuclear chemistry applications, including elemental analysis of uranium ores[20,21], surrogate nuclear debris[22], swipe samples[23] and nuclear fuel[24,25]. A 2017 study by Afgan *et. al.* implemented a

* *Corresponding Author*
[a] *Air Force Institute of Technology, 2950 Hobson Way, WPAFB, OH 45424, USA. E-mail: ashwin.rao@afit.edu*
[b] *Actinide Analytical Chemistry, Chemistry Division, Los Alamos National Laboratory, Los Alamos, NM 87545*
[c] *National Nuclear Security Administration, Washington, D.C. 20585*

handheld μ-LIBS device for quantifying minor elements in steel, achieving measurement errors comparable to those of benchtop LIBS setups and superior to those yielded by commercial XRF instruments[26]. More recently, a handheld LIBS device has been validated for rapid determination of minor elements in plutonium surrogates as well as discrimination between pure and alloyed plutonium metal[27–29]. These studies have brought to light some of the efficacy issues of portable LIBS analyzers for Pu analysis; improvement of measurement fidelity is demonstrated using chemometric techniques and machine learning techniques[30]. On the other hand, portable XRF devices have been used in a plethora of field applications from non-destructive analysis of archaeological artifacts[31,32] to detection of water contaminants and hazardous waste[33,34]. Portable XRF use for *in-situ* nuclear material analysis is less documented, but a previous investigation did prove the efficacy of such devices for detecting Pu contamination in wounds[35]. With regards to the analysis of lanthanide and transition metals, separate studies by Kirsanov *et.al.* and Labutin *et. al.* using XRF and LIBS, respectively, highlight the challenges of quantitative analysis of these metals caused by spectral interferences in the complex matrices[36,37]. Since handheld analyzers typically record spectra at lower resolutions than comparable benchtop setups, spectral interferences could have a greater impact on the accuracy of calibrations made with the handheld devices. The objective of this study is to compare the measurement fidelity of handheld LIBS and XRF devices based on (i) sensitivity and precision, and (ii) measurement time required for the identification of elements in nuclear material.

In this paper, the analytical performance of two commercial off-the-shelf (COTS) handheld elemental analyzers, the SciAps Z300 LIBS and Bruker S1 Titan XRF, are compared for detection of gallium in a cerium matrix for the first time. Cerium is a common chemical surrogate used in-lieu of plutonium; the two metals share similar electronic structures and bulk properties, and have similar spectral responses[38–41]. Accordingly, studies of cerium yield valuable insights into the behavior of plutonium. Gallium is a common metal alloyed with plutonium to stabilize its face-centered-cubic (FCC) δ phase to a malleable and machineable metal. It is critical to maintain a certain weight percent (wt %) range during alloy production to ensure a homogeneous δ phase metal is created[1,42,43]. We present calibration curves quantifying the spectral response of Ga I emission lines to changes in Ga concentration constructed from XRF and LIBS data. LoD and mean error metrics are discussed for each model to contrast the sensitivity and precision of the two devices.

2 Experimental

2.1 Sample preparation

The cerium pellet samples were prepared from Sigma Aldrich cerium oxide (99.995% CeO_2) mixed with varying weight percent concentrations of gallium oxide (99% Ga_2O_3). The powders were milled using an agate mortar and pestle, weighed to achieve the desired weight percent concentrations and then homogenized using a Fluxana MUK mixer. The mixed powder was then pressed using a 14 mm stainless steel die at 5 metric tons for 120 seconds. Pellets weighing approximately 1 gram each with 0, 0.25, 0.5, 1, 1.5, 2, 2.5, 3 and 5 wt% Ga were created for use in this experiment. The mixing and pressing equipment is shown in Fig. 1.

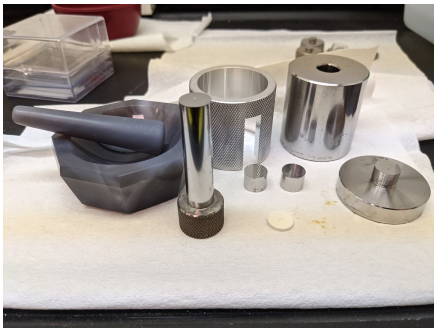

Fig. 1 Stainless steel 14mm pellet press set used for creation of samples in this study.

2.2 Spectral acquisition devices and settings

Fig. 2 SciAps Z300 portable LIBS analyzer.

Fig. 3 Bruker S1 Titan portable XRF analyzer.

A Bruker S1 Titan Model 600 portable XRF and SciAps Z300 portable LIBS analyzer, shown in Figs. 2 and 3, were utilized for spectral acquisition. The SciAps Z300 uses a 5-mJ/pulse 1064 nm Nd:YAG laser for target ablation, and directs the optical emissions from the microplasma into the on-board spectrometer system, recording a broadband spectra between 190-950 nm. The Z300 was used in gated mode with an initial gate delay of 250 ns, along with an argon pre-flush to purge air from the sample area before the ablation and recordings. All recordings are taken at atmospheric pressure. An 8x8 raster pattern was used to collect data on the samples, and every 16 spectra were averaged yielding 4 averaged spectra from a single recording. 5 recordings of each sample were taken, generating 20 separate averaged spectra at each Ga content level. The Bruker Titan uses a 4W Rh target x-ray tube at energies between 15-50 kV to generate x-rays, along with a FAST SDD detector to record the fluorescence emissions from the sample. This experiment used a generation energy at 40 kV, and a multi-phase recording over 120 seconds to generate and record a broad range of elemental x-ray excitation emissions. 20 recordings were taken of each different sample concentration,

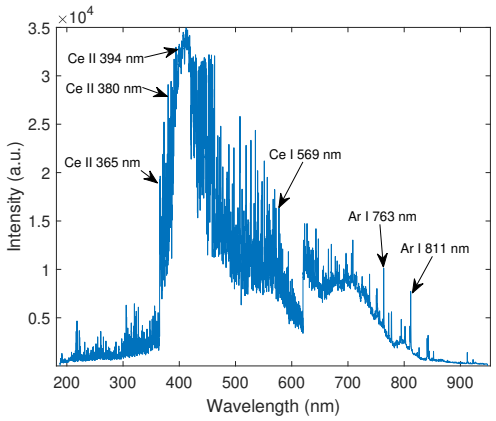

Fig. 4 Example LIBS spectrum of pure Ce sample recorded with Z300. Major Ce and Ar emissions are denoted.

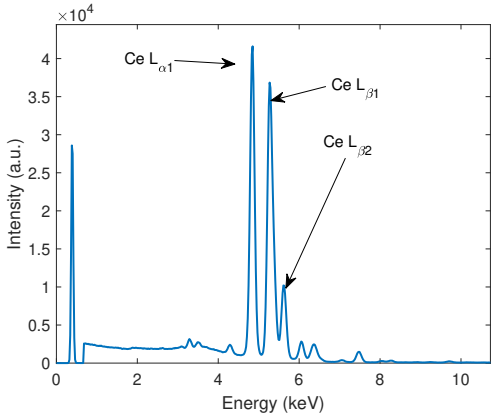

Fig. 5 Example XRF spectrum of pure Ce sample recorded with Titan S1. Three major Ce L-shell emissions (α_1, β_1, β_2) are denoted.

yielding 180 total spectra for calibrations. Example spectra from each device are displayed in Figs. 4 and 5. The example spectra clearly demonstrate the complex nature of the LIBS spectral response from heavier metals. More complex electronic structures facilitate significantly more atomic emissions over a wide range of wavelengths, posing a challenge when trying to select emission lines for calibration curves or other analytical measurements. The XRF spectrum is much less cluttered; even for heavier elements, only a few characteristic fluorescence emission lines are recorded. The three major Ce x-ray peaks, are marked in Fig. 5. The L designation signifies the emission occurs from an electron transitioning to fill a vacancy in the L-shell. The Greek letter subscripts depend on the quantum number change associated with the transition.

2.3 Analytical line selection

The strongest Ga LIBS emission exists at 417.2 nm[44]; however, the limited 0.1 nm resolution of the Z300 and plethora of Ce emissions recorded between 400-450 nm render this major Ga line unresolvable from the recorded spectra. As a result, two minor Ga I emissions at 287.4 and 294.4 nm were chosen for determination. These lines were free from other spectral interferences and demonstrated a clear relationship between intensity

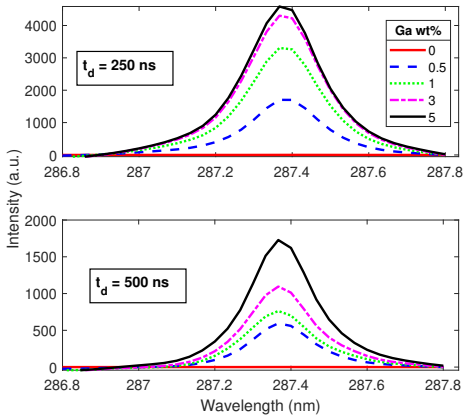

Fig. 6 Ga I 287.4 nm line intensity variation with increasing Ga content at a) 250 ns and b) 500 ns gate delay.

and Ga concentration; this is graphically demonstrated in Figs. 6 and 7. It is important to note that while the line intensity in-

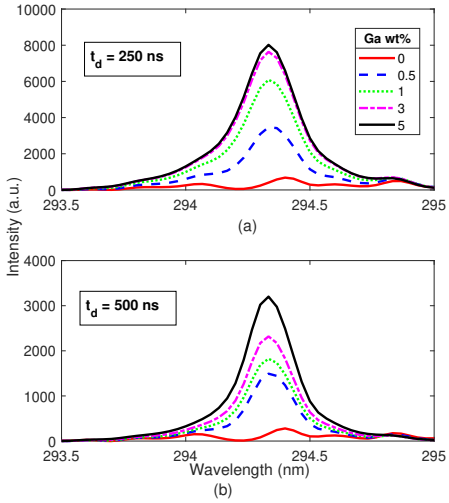

Fig. 7 Ga I 294.4 nm emission intensity variation with increasing Ga concentration at a) 250 ns and b) 500 ns gate delay.

creases with Ga content as expected, there is a significant plateau in the intensity increase past 1 wt%; the 3 and 5 wt% data points in fact have almost the same spectral response despite the significant difference in Ga content from these samples. This is an initial indication of a phenomenon known as self-absorption, in which a plasma becomes optically thick and reabsorbs certain emission wavelengths, preventing them from exiting the plasma and being recorded on a detector. This is often seen in LIBS studies and is demonstrated to be more pronounced at higher analyte concentrations[45–47]. Recent studies have recommended recording signal at longer gate delays to mitigate this effect, as it is often most pronounced in the early phases of laser-produced plasmas[48,49]. The LIBS recordings were then repeated for each sample at a later gate delay of 500 ns to evaluate this phenomenon in more detail. An initial inspection of the 3 and 5 % Ga signal intensities in Figs. 6b and 7b indicate less absorption of both emission lines at

a later gate delay compared to the 250 ns delay peaks recorded in Figs. 6a and 7a. It should be noted that the peak intensities are reduced at longer gate delays and hence could detriment the calibration fidelity. The self-absorption behavior and its effects on the LIBS calibrations are further discussed in Section 3.1.

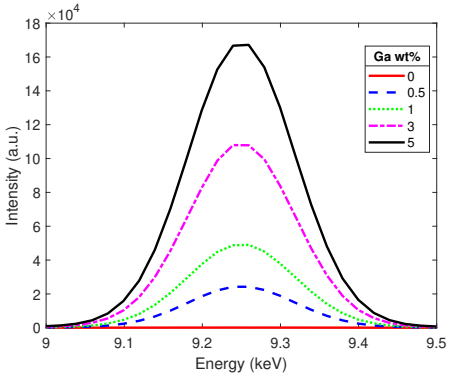

Fig. 8 Ga K_α 9.25 keV emission intensity variation with increasing Ga concentration.

The two major Ga XRF K-shell peaks were easily identified and extracted from the XRF spectra; the K_α and K_β emissions are displayed in Figs. 8 and 9 illustrating a clear, linear rise in intensity with increasing Ga concentration. Since XRF does not require the generation of a plasma to induce atomic emissions, the XRF spectra are not susceptible to photon absorption issues, unlike the LIBS spectra of the same samples. This result is an initial indication that the XRF data will yield more precise calibration curves than the corresponding LIBS data.

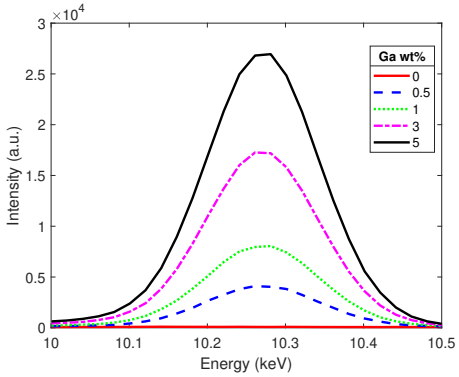

Fig. 9 Ga K_β 10.26 keV emission intensity variation with increasing Ga concentration.

3 Results

3.1 LIBS calibrations

The selected LIBS lines from the spectra at each gate delay were used to construct univariate calibration curves relating the peak intensity of each line to the Ga concentration of the sample. First, the self-absorption phenomenon was analyzed by fitting an exponential curve to the data, rather than a linear regression. The method implemented by Yage *et. al.*[45] relating the intensity of the emissions I to the analyte concentration C, a constant a and a self-absorption coefficient b was used to fit the peak intensity data. This relation is given by Eq. (1); $b \approx 1$ signifies perfectly linear behavior between intensity and concentration and the absence of self-absorption.

$$I = aC^b \tag{1}$$

Figs. 10 and 11 illustrate the curve fit applied to the Ga I 287 nm and Ga I 294 nm peak intensities at both gate delays. Visually, the self-absorption phenomenon is evident at both delay times for each line. However, it appears that the nonlinearity begins to develop at a lower concentration with a 500 ns gate delay. The 250 ns delay data remains relatively linear out to 1 wt% Ga, while at 500 ns the curve begins to bend lower around 0.5%, indicating that the level of self-absorption is more sensitive to increases in analyte concentrations at later plasma lifetimes. Table 1 lists the numerical fit coefficients for all four calibration models; the self-absorption coefficient b values indicate that increasing the gate delay reduced self-absorption by 20% with the 287 nm line, but only marginally for the 294 nm calibration. This follows the visual trend in the calibration curves showing the persistence of the phenomenon. This indicates the 294 nm line may be more susceptible to the effects of the optically thick plasma, as the bend of these calibration fits is more severely pronounced at 500 ns than

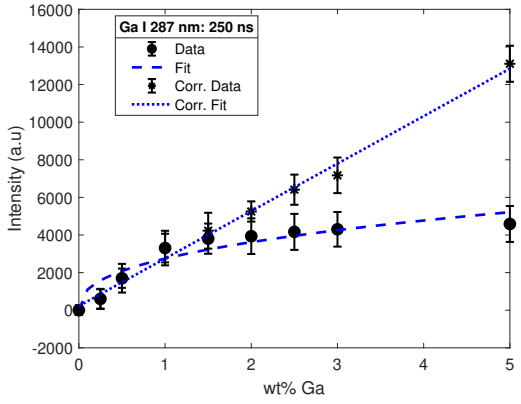

(a)

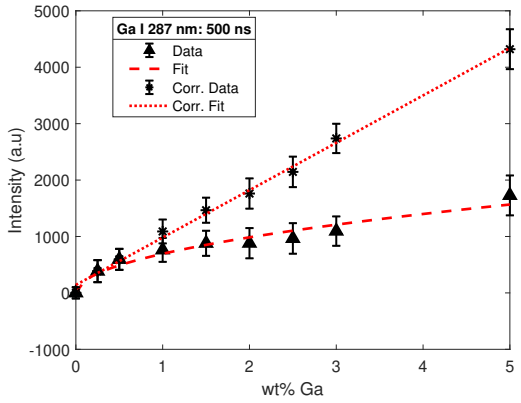

(b)

Fig. 10 Calibration curves (dashed lines) using the 287 nm peak intensity at a) 250ns and b) 500 ns gate delays showing self-absorption behavior, with their corresponding SA corrected linear curves (dotted lines).

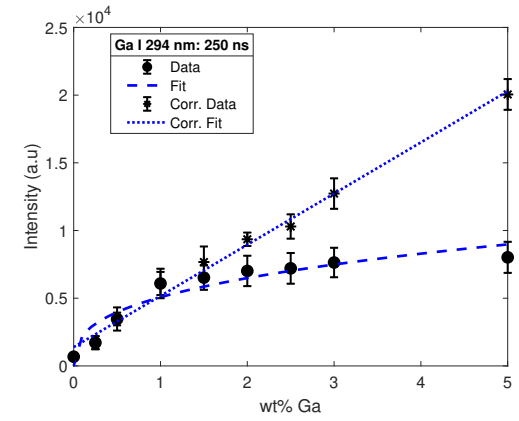

(a)

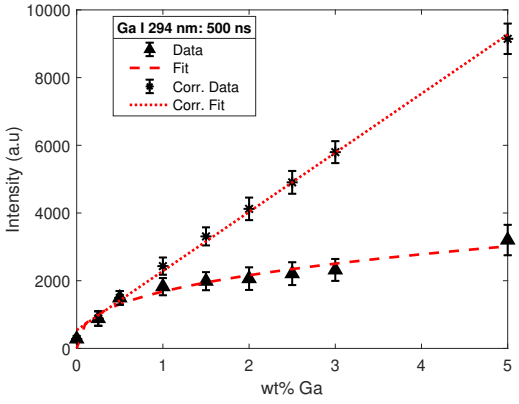

(b)

Fig. 11 Calibration curves (dashed lines) using the 294 nm peak intensity at a) 250ns and b) 500 ns gate delays showing self-absorption behavior, with their corresponding SA corrected linear curves (dotted lines).

it is for the corresponding 287 nm line calibration.

Further analysis was conducted by employing a mathematical correction to the self-absorption phenomenon. This was achieved by implementing a well documented intensity correction based on Stark broadening parameters of the selected spectral lines[46,50,51]. The correction is formulated from the understanding that the LIBS lines show significant line broadening, which typically stems from two main sources: (i) Doppler broadening occurs in a plasma when its constituent particles have a wide velocity distribution. Emission from particles moving at different velocity groups produce different Doppler shifts, and the aggregate effect of these various shifts in emissions leads to broadening of the spectral line. (ii) Stark broadening results from splitting degenerate energy levels caused by the electric fields in the plasma, which in turn splits spectral lines and also induces broadening. The Stark broadening width, referred to in this paper as the Stark fullwidth at half-maximum w_s, can be used in conjunction with other calculated plasma parameters to develop a self-absorption correction. The broadening in the observed wavelength is

$$\Delta\lambda_0 = \frac{2w_s n_e}{10^{16}}. \quad (2)$$

This equation is commonly used in LIBS modeling for the total peak FWHM λ_0 with the electron density n_e and the Stark width w_s[52]. The electron density in this equation was calculated from a non-absorbed hydrogen Balmer line found in the experimental spectra, rearranging Eq. (2) to solve for n_e. The Stark broadening of the line in the experimental spectra was calculated using a Voigt profile fit (VPF). This fitting method describes a mathematical convolution of a Gaussian and a Lorentzian function, and can be fit using the analytical expression in Eq. (3) where σ and γ refer to the Doppler and Stark broadening widths and w is the Faddeeva complex error function[53]. An example VPF of the Ga I 287.4 nm peak is illustrated in Fig. 12. This fit can generate the total peak FWHM and the Stark FWHM required to calculate SA values for the corresponding calibration using 287.4 nm line intensities.

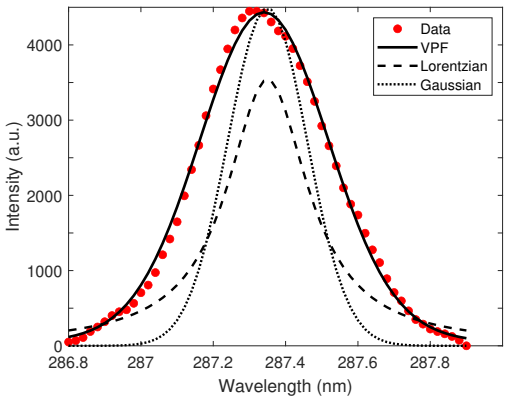

Fig. 12 Example Voigt profile fit of the Ga I 287.4 nm line, showing total fit as well as Gaussian and Lorentzian components.

$$V(\lambda,\sigma,\gamma) = \frac{Re[w(z)]}{\sigma\sqrt{2\pi}}; z = \lambda + i\gamma \quad (3)$$

The self-absorption correction (SA) is formulated by Eq. 4, noting that the measured full-width at half max (FWHM) $\Delta\lambda$ is related to the actual non self-absorbed broadening ($\Delta\lambda_0$) multiplied by SA raised to the coefficient β which is given as -0.54 in literature[46,54].

$$\Delta\lambda = \Delta\lambda_0 (SA)^{\beta} \quad (4)$$

Combining Eqs. (2) and (4) to relate the SA coefficient as a ratio of the corrected and uncorrected emission lines yields the empirical expression in Eq. (5) to calculate SA from the electron density and calculated broadening of the emission line used in the calibration curve. The corrected intensity is then calculated as the measured intensity divided by the corresponding SA value at each

Table 1 Self-absorption calibration fit parameters for all LIBS lines and gate delays.

λ_0	t_d	a	b
287 nm	250 ns	2746	0.398
	500 ns	693.2	0.507
294 nm	250 ns	5076	0.354
	500 ns	1679	0.364

point.

$$SA = \frac{I(\lambda)}{I_0(\lambda_0)} = \left(\frac{\Delta\lambda}{2w_s}\frac{10^{16}}{n_e}\right)^{\frac{1}{\beta}} \quad (5)$$

This SA value was calculated for each emission line at each gate delay with the extracted Stark widths and peak FWHMs for each peak. The original peak intensities were then divided by their corresponding SA values to generate the corrected calibration curves also shown in Figs. 10 and 11 with their uncorrected counterparts. The contrast between the uncorrected and corrected calibrations shows a clear increase in linearity of the spectral response to increasing concentration. The corrected calibration shows clear visual evidence of the efficacy of the Stark width-based correction methodology. Additionally, the contrast between the two curves visually confirms the trend of self-absorption of the Ga I lines increasing with Ga concentration present in the sample. This indicates that a higher concentration of the analyte increases the potential for a Ga emission to be reabsorbed in the microplasma.

Next, the precision of the corrected and uncorrected calibrations were evaluated by calculating the mean absolute percentage error (*MAPE*) between the fit and observed peak intensity data given by Eq. (6). This quantity estimates an average error bound for the whole calibration curve from 0 to 5 wt%.

$$MAPE = \frac{100}{n}\sum_{i=1}^{n}\left|\frac{y_i - \hat{y}_i}{y_i}\right| \quad (6)$$

The slopes of each corrected linear fit are then used to evaluate the sensitivity of the corrected models based on the limit of detection (LoD) metric given by Eq. (7).

$$LoD = \frac{3\sigma}{s} \quad (7)$$

The LoD is the IUPAC defined quantity representing the theoretical minimum analyte concentration that a given calibration model can accurately differentiate from a blank sample to within one standard deviation (σ) of error[55]. This (σ) value is determined by calculating the standard deviation of the spectral background near the emission being used for the calibration curve. The LoD is inversely proportional to the slope (s) of the linear fit; a higher slope yields a more sensitive calibration.

The aforementioned metrics were calculated for each fit and are listed in Table 2. The data clearly indicates an accuracy improvement in the models when the gate delay is extended to 500 ns, as the uncorrected calibration curves saw significant error reductions at the later time. Applying the SA correction drastically improved model precision; errors as low as 3.4% and 4.4% were achieved in conjunction with the later gate delay using the 294 and 287 nm peaks, respectively. These results clearly demonstrate the merits of the applied correction methodology for improving the efficacy of univariate calibration models. The sensitivities of each corrected model do not differ significantly when the delay is changed; in fact, for the 287 nm line the LoD actually increases 0.1% when the delay is extended. This indicates that changing the recording time mostly affects the precision of the calibrations. A potential cause for this could stem from the overall reduction in line intensity when the spectrum is capture later in the plasma lifetime. A calibration with lower intensity value data points will likely have a lower slope, which directly increases the LoD. It should be noted that the 294 nm line calibrations were significantly more sensitive than those of the 287 nm line post-correction. This peak seemingly benefited more from the applied correction when compared to the 287 nm calibrations, and yields detection limits around a tenth of a percent, which is acceptable for the problem at hand since homogoenous δ-Pu forms with 0.5 to 2.5 wt% Ga alloyed.

Table 2 LIBS univariate calibration fit metrics: *MAPE*, and LoD for each emission line and gate delay.

λ_0	t_d	Uncorr. MAPE	*Corr. MAPE*	LoD
287 nm	250 ns	38.4%	10.0%	0.60%
	500 ns	20.8%	4.4%	0.70%
294 nm	250 ns	27.4%	8.4%	0.14%
	500 ns	18.0%	3.4%	0.11%

Overall, the LIBS calibration results indicate some important trade offs to consider when choosing a gate delay for spectral acquisition with the Z300. While increasing the gate delay of the device does not significantly mitigate the effects of self-absorption on the calibration curves, it can yield calibration models with higher precision for gallium quantification. However, the sensitivity is not greatly affected and may even be detrimented in some cases due to the overall decrease in recorded spectral intensity at longer gate delays.

3.2 XRF calibrations

The selected XRF emissions discussed in Section 2.3 were used to construct calibration curves to contrast to the LIBS calibration models analyzed in the previous section. Since XRF doesn't generate a plasma and induces electronic emissions by perturbing individual electrons rather than the bulk sample, there are no physical phenomena such as self-absorption to affect the intensity data collected by this device. This is clearly demonstrated in the calibration curves for the K_α and K_β peak intensities in Figs. 13 and 14, which demonstrate nearly perfect linear fits to the data points. The *MAPE* and LoD values calculated for each calibration are listed in Table 3.

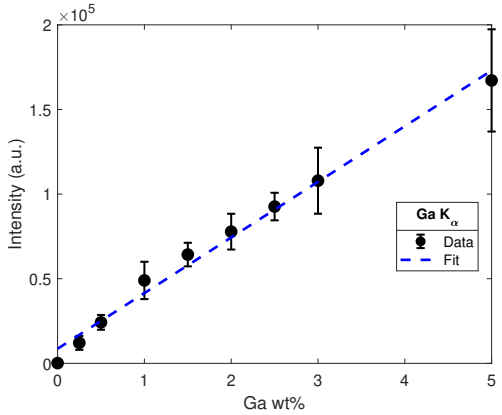

Fig. 13 Univariate calibration curve using Ga K_α 9.25 keV peak intensity.

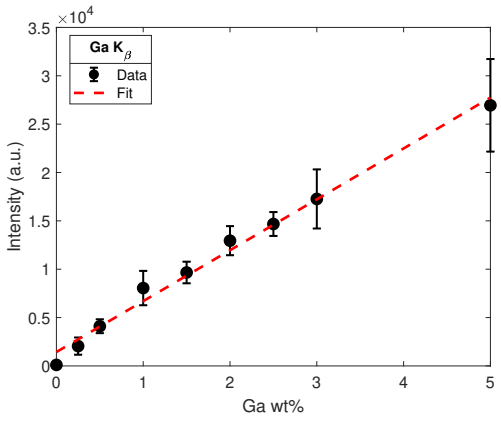

Fig. 14 Univariate calibration curve using Ga K_β 10.26 keV peak intensity.

The XRF calibrations yield a mean error percentage of the same order of magnitude as the corrected LIBS calibrations, with less than 10 percent error shown by both models. While the 500 ns delay LIBS calibrations are still slightly more accurate, a significant overall improvement over the LIBS calibrations is attributed to the LoD values for the XRF models. The LoDs for the K_α and K_β curves reach 20 and 80 ppm Ga, respectively. To achieve such low detection limits with LIBS, either a large laboratory laser and spectrograph setup are needed, or complex machine learning algorithms are required for analysis of the LIBS spectra. Additionally, the effects of self-absorption in a LIBS plasma often hamper the sensitivities of calibration models, even when the intensity values are corrected. The distinctly linear response to concentration yielded by the fluorescence technique created a robust model with superlative responsivity to changes in Ga concentration. This

Table 3 XRF univariate calibration fit metrics: *MAPE* and LoD for each emission peak.

Peak	*MAPE*	LoD
K_α	9.8 %	0.002%
K_β	8.3%	0.008%

result points to significant advantages of the portable XRF for the detection of gallium in a cerium matrix. The method provides a significantly less complex data set for chemometric analysis, and can circumvent the many physics processes which occur in a laser-induced plasma which can detriment the accuracy of LIBS spectra based quantitative calibration models. It should be noted, however, that the LoDs calculated based on the IUPAC definition are a theoretical estimate; to verify this figure one would have to take a recording of a sample with the same analyte concentration as the LoD and verify that the recorded peak is distinguishable from the blank sample. These calculated LoDs are well below the lowest analyte concentrations tested in this study, however, it is not inconceivable that the XRF device would detect Ga at concentrations lower than 0.1% due to its markedly more linear response and low spectral background deviation. With this in mind, the XRF was able to yield the better quantitative model for Ga quantification in this study. Drawbacks to note of the XRF device are the durability of the device itself and the data acquisition time. While a LIBS measurement can be conducted in less than a second, the XRF needs a timescale of minutes to generate reliable spectra. Additionally, the Bruker Titan relies on a delicate silicon drift detector (SDD), which can be sensitive to changes in temperature or damage from impact shocks to the device. Furthermore, for the eventual application to analysis of Pu alloys, one must also consider the potential effects of gamma radiation on the SDD, as this could affect lifetime and longer-term usability of the portable XRF. While this study does not seek to chose one device as the superlative method for potential elemental analysis in Pu alloys, the results of this investigation bring up several important factors to consider when choosing these devices for analysis of nuclear material or related endeavors.

4 Conclusions

This novel investigation comparing two COTS portable elemental analyzers served to discover potential points of consideration when evaluating handheld LIBS or XRF devices for elemental quantification. The complexity of the electronic emissions seen in lanthanide and actinide metals, coupled with deleterious plasma effects such as self-absorption, limit the performance of a handheld LIBS device for quantification of gallium in plutonium or cerium. While precision can be improved using a self-absorption correction and a later delay time to reduce errors down to the low single percent range, the corrected sensitivity is not greatly affected by increasing gate delay. In fact, the reduction in recording signal could potentially increase the detection limits at later delay times. The XRF device yielded much cleaner calibration fits with comparable errors on the same order of magnitude as the corrected LIBS fits. The XRF calibrations saw immense improvements in sensitivity, showing LoDs as low as 20 ppm for the detection of Ga. Although the XRF needs longer timescales for data acquisition and relies on more sensitive components for detection, it produced quantitative models with objectively superior sensitivity for the problem examined in this experimental work.

Conflicts of interest

There are no conflicts to declare.

Acknowledgements

This work was supported by the Defense Threat Reduction Agency under funds from the Nuclear Science and Engineering Research Center (NSERC). This document is cleared for public release under 88ABW-2021-0732 and LA-UR-21-29174.

Notes and references

1 D. Clark, S. Hecker, G. Jarvinen and M. Neu, *Chemistry of the Actinide and Transactinide Elements*, Springer, Dordecht, 2008.

2 M. Krachler and R. Alvarez-Sarandes, *Microchemical Journal*, 2016, **125**, 196 – 202.

3 Radboud, *General Instrumentation*, `https://www.ru.nl/science/gi/facilities-activities/elemental-analysis/icp-oes/`, 2018, Accessed on 2019-04-16.

4 G. L. Donati, R. S. Amais and C. B. Williams, *J. Anal. At. Spectrom.*, 2017, **32**, 1283–1296.

5 E. Simon, A. Vidic, M. Braun, I. Fabian and B. Tothmeresz, *Environ Sci Pollut Res Int*, 2012, 917–24.

6 R. Falciani, E. Novaro, M. Marchesini and M. Gucciardi, *J. Anal. At. Spectrom.*, 2000, **15**, 561–565.

7 C. Streli, P. Wobrauschek and P. Kregsamer, *Encyclopedia of Spectroscopy and Spectrometry (Third Edition)*, Academic Press, Oxford, Third Edition edn, 2017, pp. 707 – 715.

8 D. Hahn and N. Omenetto, *Applied Spectroscopy*, 2010, **64**, 335–66.

9 D. W. Hahn and N. Omenetto, *Appl. Spectrosc.*, 2012, **66**, 347–419.

10 B. T. Manard, E. M. Wylie and S. P. Willson, *Applied Spectroscopy*, 2018, **72**, 1653–1660.

11 P. Porizka, *PhD thesis*, Brno University of Technology, 2014.

12 N. Yang, N. Eash, J. Lee, M. Martin, Y.-S. Zhang, F. Walker and J. E. Yang, *Soil Science*, 2010, **175**, 447–452.

13 J. L. Gottfried, R. S. Harmon, F. C. D. Lucia and A. W. Miziolek, *Spectrochim Acta B*, 2009, **64**, 1009 – 1019.

14 E. Negre, V. Motto-Ros, F. Pelascini, S. Lauper, D. Denis and J. Yu, *J. Anal. At. Spectrom.*, 2015, **30**, 417–425.

15 M. F. Alberghina, R. Barraco, M. Brai, T. Schillaci and L. Tranchina, *Journal of Physics: Conference Series*, 2011, **275**, 012017.

16 M. B. Shattan, D. J. Miller, M. T. Cook, A. C. Stowe, J. D. Auxier, C. Parigger and H. L. Hall, *Appl. Opt.*, 2017, **56**, 9868–9875.

17 J. Sirven, A. Pailloux, Y. Baye, N. Coulon, T. Alpettaz and S. Gosse, *J. Anal. At. Spectrom.*, 2009, **24**, 451–459.

18 A. M.F, R. Barraco, M. Brai, D. Fontana and L. Tranchina, *Periodico di Mineralogia*, 2015, **84**, 569–589.

19 D. Discenza, A. Keimowitz and N. Fitzgerald, *J. Environ. Anal. Chem.*, 2014, **1**, 103.

20 J. Klus, P. Mikysek, D. Prochazka, P. Porizka, P. Prochazková, T. T. J. Novotny and, M. S. K. Novotny and and J. Kaiser, *Spectrochim. Acta B*, 2016, **123**, 143–149.

21 Y. Kim, B. Han, H. S. Shin, H. D. Kim, E. C. Jung, J. H. Jung, and S. H. Na, *Spectrochim. Acta B*, 2012, **75**, 190–193.

22 M. B. Shattan, M. Gragston, Z. Zhang, I. John D. Auxier, K. G. McIntosh and C. G. Parigger, *Applied Spectroscopy*, 2019, **73**, 591–600.

23 R. Chinni, D. A. Cremers and R. Multari, *Appl. Opt.*, 2010, **49**, C143–C152.

24 A. Sarkar, D. Alamelu and S. K. Aggarwal, *Appl. Opt.*, 2008, **4**, G58–G64.

25 S. Dhara and N. Misra, *TrAC Trends in Analytical Chemistry*, 2019, **116**, 31 – 43.

26 M. S. Afgan, Z. Hou and Z. Wang, *J. Anal. At. Spectrom.*, 2017, **32**, 1905–1915.

27 A. P. Rao, M. T. Cook, H. L. Hall and M. B. Shattan, *Atoms*, 2019, **7**, 84.

28 A. Rao, J. Auxier, D. Vu and M. Shattan, Laser Applications to Chemical, Security and Environmental Analysis, 2020, p. LM1A.2.

29 A. P. Rao, P. R. Jenkins, J. D. Auxier II and M. B. Shattan, *J. Anal. At. Spectrom.*, 2021, **36**, 399–406.

30 A. P. Rao, P. R. Jenkins, D. M. Vu, J. D. Auxier II, A. K. Patnaik and M. B. Shattan, *Anal. Methods*, 2021, **13**, 3368–3378.

31 A. M. Hunt and R. J. Speakman, *Journal of Archaeological Science*, 2015, **53**, 626 – 638.

32 A. Longoni, C. Fiorini, P. Leutenegger, S. Sciuti, G. Fronterotta, L. Strüder and P. Lechner, *Nuclear Instruments and Methods in Physics Research Section A: Accelerators, Spectrometers, Detectors and Associated Equipment*, 1998, **409**, 407 – 409.

33 F. Melquiades and C. Appoloni, *Journal of Radioanalytical and Nuclear Chemistry - J RADIOANAL NUCL CHEM*, 2004, **262**, 533–541.

34 D. J. Kalnicky and R. Singhvi, *Journal of Hazardous Materials*, 2001, **83**, 93 – 122.

35 H. Yoshii, K. Yanagihara, H. Imaseki, T. Hamano, H. Yamanishi, M. Inagaki, Y. Sakai, N. Sugiura, O. Kurihara and K. Sakai, *PLOS ONE*, 2014, **9**, 1–7.

36 D. Kirsanov, V. Panchuk, A. Goydenko, M. Khaydukova, V. Semenov and A. Legin, *Spectrochimica Acta Part B: Atomic Spectroscopy*, 2015, **113**, 126–131.

37 T. A. Labutin, S. M. Zaytsev, A. M. Popov and N. B. Zorov, *Journal of Analytical Atomic Spectrometry*, 2016, **31**, 2223–2226.

38 F. E. Gibbs, D. L. Olson and W. Hutchinson, *AIP Conference Proceedings*, 2000, **532**, 98–101.

39 H. Zheng, F.-Y. Yueh, T. Miller, J. Singh, K. E. Zeigler and J. C. Marra, *Spectrochim Acta B*, 2008, **63**, 968–974.

40 M. Moore and Y. Tao, *Aerosol Physics Considerations for Using Cerium Oxide CeO2 as a Surrogate for Plutonium Oxide PuO2 in Airborne Release Fraction Measurements for Storage Container Investigations*, 2017.

41 J. C. Marra, A. D. Cozzi, R. A. Pierce, J. M. Pareizs, A. R. Jurgensen and D. M. Missimer, in *Cerium as a Surrogate in the Plutonium Immobilized Form*, John Wiley & Sons, Ltd, 2012, ch. 36, pp. 381–388.

42 P. Söderlind, F. Zhou, A. Landa and J. Klepeis, *Scientific Reports*, 2015, **5**, 15958.

43 M. Steinzig and F. H. Harlow, *MRS Proceedings*, 1999, **538**,.

44 A. Kramida, Y. Ralchenko and J. Reader, *NIST Atomic Spectra Database*, `https://physics.nist.gov/asd`.

45 H. Yage, X. Wang, G. Shuai, A. Li, X. Xu, N. Wazir, D. Chunjie, T. Lu, L. Xie, M. Zhang, Y. Hao, W. Guo and R. Liu, *Applied Optics*, 2019, **58**, 422.

46 F. Rezaei, P. Karimi and S. H. Tavassoli, *Applied Physics B*, 2013, **114**,.

47 A. K. Patnaik, Y. Wu, P. S. Hsu, M. Gragston, Z. Zhang, J. R. Gord and S. Roy, *Optics express*, 2018, **26**, 25750–25760.

48 Y. Tang, S. Ma, Y. Chu, T. Wu, Y. Ma, Z. Hu, L. Guo, X. Zeng, J. Duan and Y. Lu, *Opt. Express*, 2019, **27**, 4261–4270.

49 A. P. Rao, M. Gragston, A. K. Patnaik, P. S. Hsu and M. B. Shattan, *Optics express*, 2019, **27**, 33779–33788.

50 F. Rezaei, G. Cristoforetti, E. Tognoni, S. Legnaioli, V. Palleschi and A. Safi, *Spectrochimica Acta Part B: Atomic Spectroscopy*, 2020, **169**, 105878.

51 H. Jiajia, L. Zhang, Z. Yang, W. Zhe, Y. Zhang, M. Weiguang, D. Lei, Y. Wangbao, X. Liantuan and J. Suotang, *Plasma Science and Technology*, 2019, **21**, 034016.

52 H. Griem, *Spectral Line Broadening by Plasmas*, Elsevier Science, 2012.

53 M. Zaghloul, *Software*, 2011, **38**, 1–22.

54 A. El Sherbini, T. M. El Sherbini, H. Hegazy, G. Cristoforetti, S. Legnaioli, V. Palleschi, L. Pardini, A. Salvetti and E. Tognoni, *Spectrochimica Acta Part B: Atomic Spectroscopy*, 2005, **60**, 1573–1579.

55 G. Long and J. Winefordner, *Analytical Chemistry - ANAL CHEM*, 2008, **55**,.